Philosophical Magazine
Publication details, including instructions for authors and subscription information:
http://www.tandfonline.com/loi/tphm20

Identification of a strain-aging model accounting for Lüders behavior in a C-Mn steel

A. Marais [a b], M. Mazière [a], S. Forest [a], A. Parrot [b] & P. Le Delliou [b]

[a] Mines ParisTech, Centre des Matériaux, CNRS UMR7633, BP 87, 91003 Evry Cedex, France

[b] EDF R&D/MMC, Site des Renardières, 77818 Moret s/Loing Cedex, France

Version of record first published: 04 Jul 2012.

To cite this article: A. Marais, M. Mazière, S. Forest, A. Parrot & P. Le Delliou (2012): Identification of a strain-aging model accounting for Lüders behavior in a C-Mn steel, Philosophical Magazine, 92:28-30, 3589-3617

To link to this article: http://dx.doi.org/10.1080/14786435.2012.699687

Philosophical Magazine
Vol. 92, Nos. 28–30, 1–21 October 2012, 3589–3617

Taylor & Francis
Taylor & Francis Group

Identification of a strain-aging model accounting for Lüders behavior in a C-Mn steel

A. Marais[ab]*, M. Mazière[a], S. Forest[a], A. Parrot[b] and P. Le Delliou[b]

[a]*Mines ParisTech, Centre des Matériaux, CNRS UMR7633, BP 87, 91003 Evry Cedex, France;* [b]*EDF R&D/MMC, Site des Renardières, 77818 Moret s/Loing Cedex, France*

(*Received 3 December 2011; final version received 10 May 2012*)

Strain-aging constitutive models are suitable to simulate the formation and propagation of Lüders bands in complex specimens and components. The identification of the corresponding material parameters is difficult because the strain localization phenomena associated with the Lüders behavior must be taken into account. The spurious mesh dependence of standard finite element simulations of Lüders band propagation is illustrated in the present work and removed using a strain gradient plasticity model. Furthermore the gradient approach introduces a characteristic size corresponding to the finite dimension of the Lüders band front as observed from strain field measurements. The parameters are identified from the experimental measurement of the peak stress and plastic strain carried by the band for a C-Mn steel over a temperature range from −150°C to room temperature and for several strain rates. The validity of the model is tested on 3D simulations of the Lüders band propagation in a strain gradient plasticity medium.

Keywords: Lüders bands; computational mechanics; strain gradient plasticity; strain localization; parameter identification; static strain aging

1. Introduction

The sharp yield point phenomenon was discovered in 1842 by Piobert in mild steel sheets hit by bullets [1]. Also described by Lüders in 1860 [2], it occurs in body-centered cubic (bcc) polycrystals at room temperature, and has often been observed in ferritic steels [3]. Many structural materials are subject to strain aging that can induce inhomogeneous yielding. The transition from elastic to plastic deformation is characterized by a material instability known as the Lüders phenomenon. The macroscopic effect of the instability is the emergence and subsequent propagation of plastic deformation bands. In a tensile sample loaded at constant cross-head velocity, it is associated with a band of localized dislocation activity traveling along the sample. The band nucleation, usually at one grip, corresponds to a drop in stress, from the upper yield point to the lower yield point. The plastically strained area then spreads along the sample. A clear band front separates this area from the undeformed one, into which it propagates, until the sample is uniformly stretched

*Corresponding author. Email: anthony.marais@mines-paristech.fr

ISSN 1478–6435 print/ISSN 1478–6443 online

http://dx.doi.org/10.1080/14786435.2012.699687
http://www.tandfonline.com

at the so-called Lüders strain level. From this point onwards, the deformation proceeds uniformly in the sample.

Many observations of the Lüders phenomenon are available in the literature. It has been mainly observed in iron and steels [4–11]. However, only limited attention has been paid to the description of the band front zone. The interface located between the non-deforming and the deformed area seems, at first glance, to be a zone of discontinuity of plastic strain. Detailed observations of the front by means of recent strain field measurement methods reveal that this interface is rather diffuse and may involve a large number of grains in the transition zone [12]. The characteristic width of the band front has been measured in [13,14]. This length is estimated to be several hundred micrometers by optical observations. Over this distance the plastic strain varies continuously from the maximal value inside the band to zero. The digital image correlation is the best-suited method to investigate the Lüders phenomenon, as proved in [5,6,12,15]. This technique allows us to collect information about the orientation, propagation and the level of plastic strain of Lüders bands. It is also known that the Lüders strain is strongly sensitive to grain size [16,17].

Cottrell and Bilby [18] attributed the upper yield stress in steels to the pinning of dislocations by carbon and nitrogen atoms which naturally tend to form "atmospheres" around them. They postulated that initial yielding requires a higher stress in order to pull the dislocations out of their atmospheres. Once released, the dislocations can be moved by a lower stress. The pinning effect of interstitial impurities is widely accepted for several reasons including the reappearance of the Lüders effect following mild heat treatment which allows these atoms to migrate and repin the dislocations, which is characteristic of static strain aging.

The simulation of Lüders band formation and propagation in testing samples and industrial components requires the definition of suitable nonlinear constitutive equations capturing the effect of static strain aging. Two main classes of models have been used for that purpose. The first class is based on the classical elastic–viscoplastic model with von Mises plasticity and phenomenological equations for softening and hardening behavior, as suggested in [19] where the Lüders band propagation is explicitly simulated based on the finite element method. The second class of models takes into account the physical origin of strain aging, i.e. the pinning of dislocations by solute atmospheres that diffuse during straining or waiting, by means of an internal variable called the aging time [20–23]. A model based on mesoscale field dislocation mechanics is presented for the dislocation–solute interaction and applied to the study of strain aging in [24,25].

The finite element method has been applied in the case of the Lüders effect to accurately reproduce experimental tensile tests and to validate material models and parameters. Some simulations have been performed in 2D [3,8,19] and in 3D [5]. However, no indication was given in these contributions of a systematic identification strategy of the material parameters from experimental data. The main difficulty of material parameter identification of a strain-aging models lies in the fact that strain localization phenomena must be taken into account, which requires finite element simulations. Also, the existing literature does not mention the possible mesh dependency of the finite element results when simulating Lüders band formation and propagation.

The objective of the present work is to propose a systematic methodology of identification of a static strain-aging model from the experimental tensile curves for a C-Mn steel over a large range of temperatures. The originality of the method is that strain localization phenomena are taken into account but the number of finite element simulations during the parameter optimization is limited to a minimum. For that purpose, we will show that some parameters can be calibrated from volume element simulations and that only a limited number of finite element simulations are finally needed to validate the whole procedure. An original contribution of this work is to show that finite element simulations of Lüders band formation propagation based on standard finite element methods, as used in previous simulations in the literature, are strongly mesh dependent, especially regarding the determination of the plateau stress and Lüders strain. To get rid of mesh dependency in our simulations, a regularization method is introduced based on the micromorphic generalized continuum [26]. Motivations for such a regularization procedure originate from contributions in [22,27–29] which advocate that strain gradient plasticity effects play a significant role in the propagation of the Lüders band front. The proposed model contains an intrinsic length that accurately accounts for the finite width of the Lüders band front, as observed from strain field measurements from the literature [12] and from this work.

This work is divided into four parts. In Section 2, the experimental aspects are presented regarding the material and the mechanical tests. The digital image correlation method has been used to highlight the Lüders phenomenon, see [5,15]. Section 3 starts with a theoretical mechanical analysis of a Lüders band within the rate-independent framework. Then, a phenomenological elasto-plastic model is used to simulate Lüders band formation and propagation. As suggested in [19] the strain localization of the Lüders band is induced by the introduction of a phenomenological local softening behavior. The nonlinear material behavior is modeled using a classical von Mises plasticity model. The strong mesh dependence of the results is illustrated using different kinds of mesh topology. The introduction of viscosity effects slightly alleviates the pathological behavior but is not sufficient to get rid of the spurious mesh dependence. In Section 4, the main purpose is to propose mesh objective simulations of Lüders band propagation by incorporating a finite size band front. Finally in Section 5, an original strategy of identification is proposed for a constitutive model accounting for mechanical static strain aging. It is applied to a C-Mn steel for temperatures ranging from -150°C to room temperature. The model is able to reproduce the peak and plateau stresses, the Lüders strain and the associated strain rate sensitivity from $10^{-5}\,s^{-1}$ to $10^{-1}\,s^{-1}$. The identification is validated on 2D and 3D simulations of Lüders band propagation in Section 5.5.

2. Experimental

2.1. *Material*

All experiments were conducted on a C-Mn steel (A42) whose chemical composition is detailed in Table 1. This alloy is very sensitive to strain aging due to the small Al content. The material is extracted from a seamless secondary coolant pipe obtained by a circular rolling process. The microstructure is composed of ferrite and pearlite in

Table 1. Chemical composition (weight percent) of the carbon manganese steel A42 used in this work.

Steel	C	N	Al	Si	P	S	V	Cr	Mn	Ni	Cu	Nb	Mo	Sn
A42	0.15	0.004	0.019	0.19	0.034	0.021	<0.002	0.034	0.73	0.05	0.041	<0.002	0.006	0.003

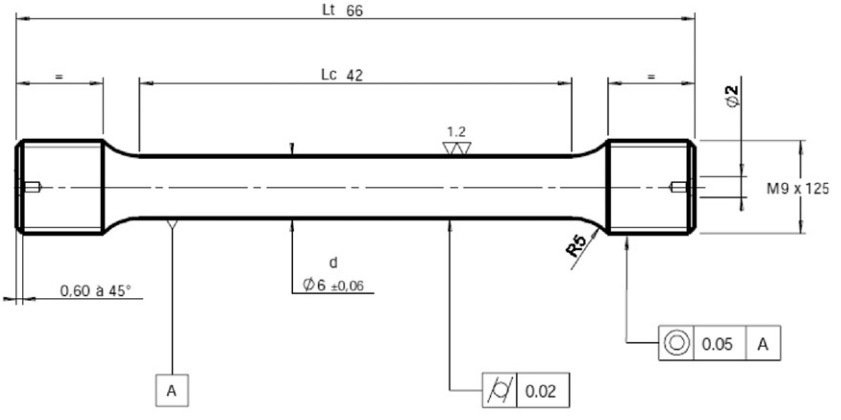

Figure 1. Tensile test specimen (TC6).

alternate bands along planes parallel to the axial and circumferential directions. The crystallographic texture was not analyzed. However, the section of the cylindrical tensile specimen remains circular up to fracture strain. So, the mechanical behavior is rather isotropic at least in the long and short transverse plane. By extension, we considered the mechanical behavior as fully isotropic, weakly affected by the morphological texture, nor by the crystallographic texture.

2.2. *Mechanical response*

The tensile tests were conducted using a 25 kN load cell servo-hydraulic testing machine. The cylindrical tensile test specimen geometry is given in Figure 1. The diameter of the gauge section of the cylindrical specimen was 6 mm and the gauge length was 42 mm. Loading of the specimens was applied quasi-statically by prescribing a constant velocity for the stroke of the actuator in the testing device. The velocities of the actuator were calculated to prescribe nominal gauge length strain rates of 10^{-5}, 10^{-3} and $10^{-1}\,s^{-1}$. The average strain over a 25 mm length at the center of the specimen is measured using an extensometer. Six different temperatures (-150, -100, -50, 0 and 20°C) were investigated.

The results of tensile tests are presented in Figures 2–3 and Tables 2–3. The upper yield point is the maximum stress following the linear elastic regime where the deformation is expected to be still homogeneous. At this point, the Lüders bands nucleate locally in the specimen and the load drops to the lower yield point.

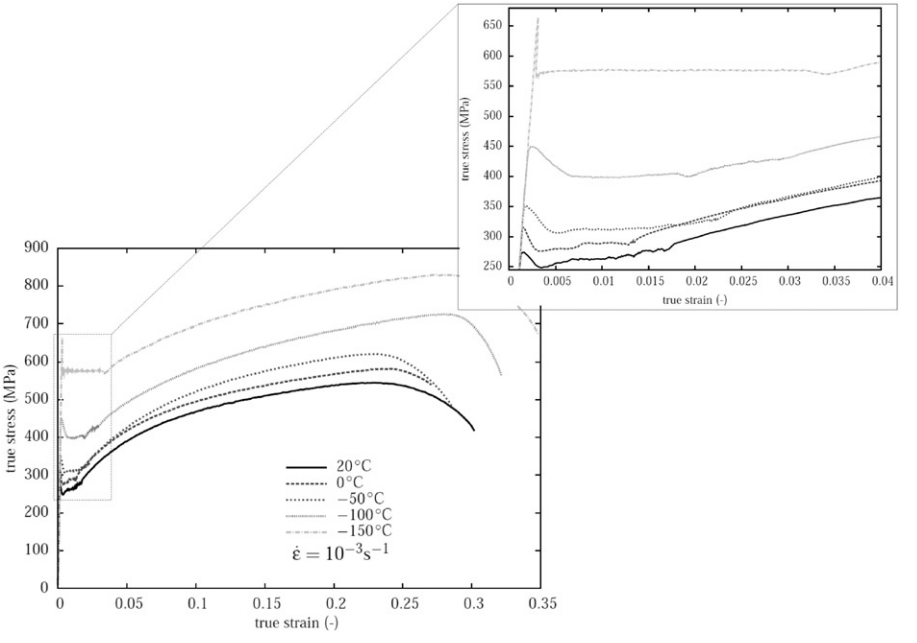

Figure 2. Tensile test stress–strain results from extensometer at $10^{-3}\,s^{-1}$.

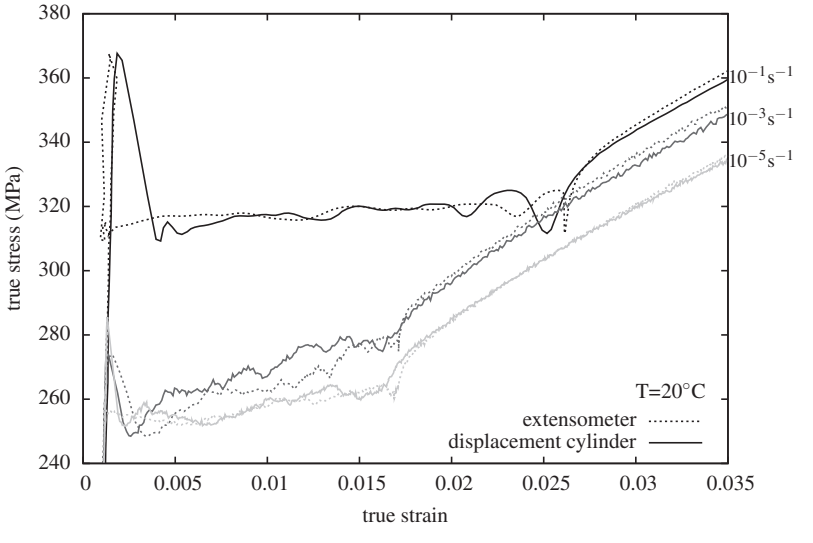

Figure 3. Tensile stress–strain curves at room temperature at three different strain rates.

Further stretching occurs at a relatively constant load due to the propagation of Lüders bands. The deformation in the specimen is strongly inhomogeneous at this time. Under continued extension, the Lüders bands spread over the whole length of the specimen until the entire test gauge length has yielded. This happens at a strain

Table 2. Tensile test results for different temperatures at $10^{-3}\,s^{-1}$.

Temperature (°C)	Upper yield (MPa)	Lower yield (MPa)	Lüders strain (%)
20	273.8	248.4	1.55
0	315.1	275.7	1.18
−50	351.2	306.8	2.04
−100	449.2	397.7	2.67
−150	663.9	569.7	3.1

Table 3. Tensile test results for different strain rates at room temperature.

Strain rate (s^{-1})	Upper yield (MPa)	Lower yield (MPa)	Lüders strain (%)
10^{-5}	285.4	251.7	1.54
10^{-3}	273.8	248.4	1.55
10^{-1}	367.6	309.2	2.42

level called the Lüders strain. Beyond this strain level, deformation is homogeneous. The material exhibits a yield point at all tested strain rates and in general both the upper and lower points increase while increasing the strain rate. On the other hand, the upper and lower points increase with decreasing temperature. By looking closely at the curves of Figure 2, one can notice the existence of a plateau at all temperatures. The plateau length is two times higher at −150°C than at room temperature. The height of the peak increases also when the temperature decreases. At room temperature, the height of the peak with respect to the plateau stress is around 25 MPa whereas at −150°C, it is almost 95 MPa.

Figure 3 highlights the importance of the strain calculation method. The gauge length extensometer is 25 mm whereas the specimen gauge length is 42 mm. Therefore if the Lüders band initiates outside of the extensometer, the strain evolution due to Lüders strain localization is not recorded. The stress drop just after the peak is sharp. If the strain is estimated by using the stroke displacement, the whole specimen gauge length is accounted for and the whole propagation of the Lüders bands is captured. The strain based on stroke displacement is calculated using a correction of the machine stiffness estimated from the elastic strain measured using the extensometer.

2.3. *Strain field measurements*

Full field images of the sample surface were collected and a DIC technique with the help of the VIC3D software (VIC3D and Correlated Solutions Incorporated) was used to evaluate strain fields. The 3D system used two 4-megapixel CCD cameras connected by firewire to a data collection PC. Frames rates up to 4 Hz were achieved and image collection was synchronized to load frame output values of load and

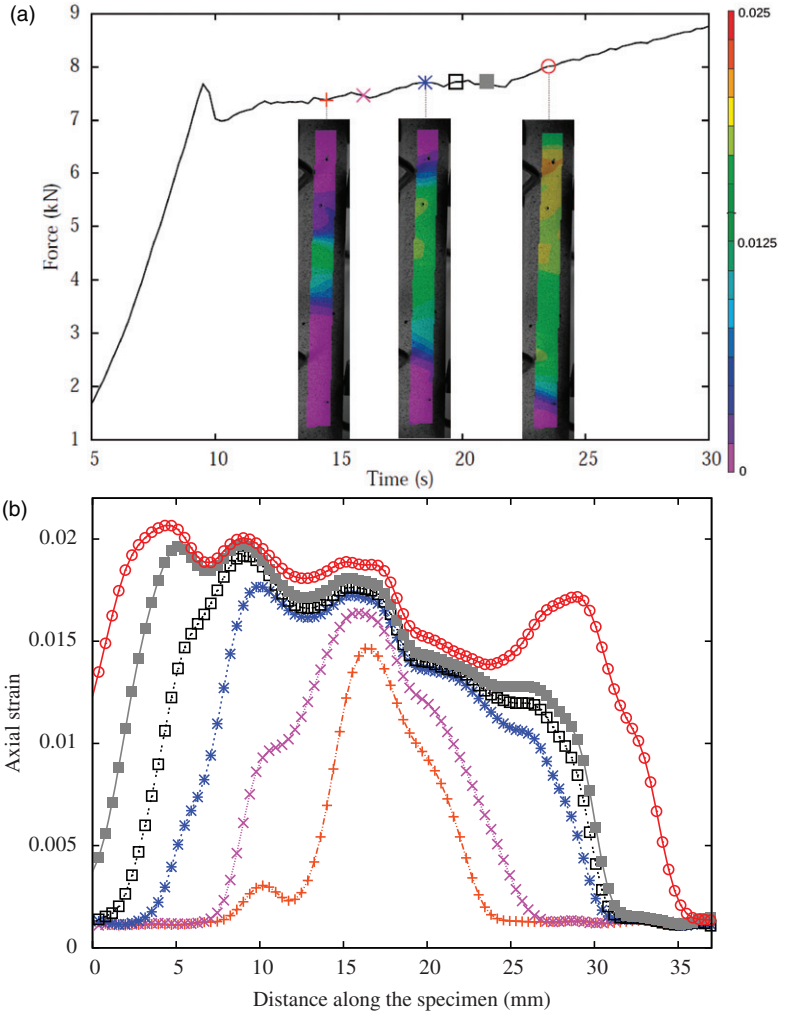

Figure 4. (a) Force–time curve for one DIC test and the full field axial strain profiles in the vertical direction at three different time steps in the vertical direction for a specimen tested at a strain rate of $10^{-3}\,s^{-1}$; (b) axial strain profiles along a vertical line taken from the strain fields at six time steps.

cross-head displacement. The camera has a fixed focal length of 50 mm. The strain analysis was based on 15 by 15 pixel facet sizes for the correlation and a step size of 6 pixels between subset centers. The DIC technique provides useful information about the level of strain in a Lüders band, the orientation of the Lüders band and the band front. The Lüders strain is determined in the same way as [5] with DIC.

Figure 4 shows the contour of the axial strain component at three different time steps, during the propagation of the Lüders band in a test at $10^{-3}\,s^{-1}$ strain rate and room temperature. Some strain profiles along a vertical line cutting through the Lüders bands are also presented. The band initiates in the middle of the specimen.

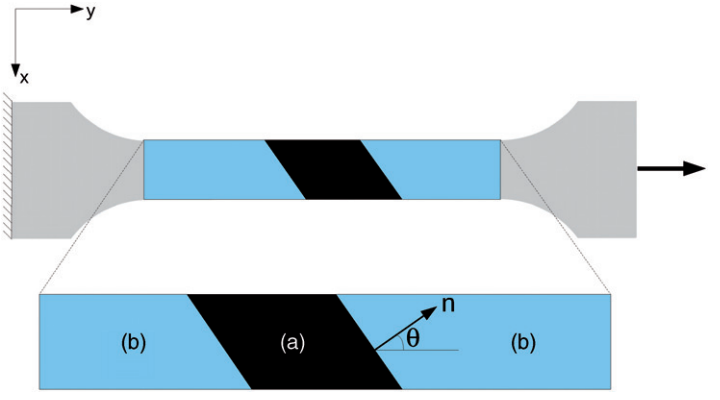

Figure 5. Mechanical state for a material domain containing a Lüders band in a tensile test.

The band front is oriented at about 55° from the tensile axis and moves on each side until it fills the whole sample. The strain profiles display several bumps indicating the possible formation of multiple Lüders bands or change of band plane which may occur in cylindrical specimens. There is no real strain discontinuity but rather a smooth front band zone extending over a few millimeters.

3. Simulation of the Lüders phenomenon

3.1. *Mechanical analysis of a Lüders band*

Figure 5 shows a region of a material sample including a Lüders band in a given area denoted by (a). It is assumed that the remainder of the specimen, denoted by (b), is not affected by the plastic strain localization. The existence of two parallel perfect interfaces is assumed in this first simple mechanical analysis. The stress and strain states are studied in the case of overall uniaxial tension. The normal vector $\underline{\boldsymbol{n}}$ located at the interface (a)/(b) admits the following components in the coordinate frame (x, y) indicated in the figure:

$$\underline{\boldsymbol{n}} = \begin{bmatrix} -\sin\theta \\ \cos\theta \\ 0 \end{bmatrix} \tag{1}$$

where θ is the angle between the y-axis and the normal $\underline{\boldsymbol{n}}$.

3.1.1. *Stress state*

The condition of continuity of the traction vector at the interface is written as

$$[\![\underset{\sim}{\boldsymbol{\sigma}}]\!] \cdot \underline{\boldsymbol{n}} = 0 \tag{2}$$

where the double brackets denote the discontinuity at an interface point. The homogeneous Lüders stress in the band is called $\underset{\sim}{\boldsymbol{\sigma}}^a$, and $\underset{\sim}{\boldsymbol{\sigma}}^b$ denotes the homogeneous

stress tensor outside the band corresponding to a tensile stress state σ in the y-direction. Then Equation (2) implies:

$$\underset{\sim}{\boldsymbol{\sigma}}^b.\underline{\boldsymbol{n}} = \begin{bmatrix} 0 \\ \sigma\cos\theta \\ 0 \end{bmatrix} = \underset{\sim}{\boldsymbol{\sigma}}^a \cdot \underline{\boldsymbol{n}} = \begin{bmatrix} \sigma^a_{xy}\cos\theta \\ \sigma^a_{yy}\cos\theta \\ 0 \end{bmatrix} \tag{3}$$

from which we deduce that $\sigma^a_{yy} = \sigma$, $\sigma^a_{xy} = 0$. The presence of free lateral surfaces also implies that $\sigma^a_{xx} = 0$. As a result, we obtain $\underset{\sim}{\boldsymbol{\sigma}}^a = \underset{\sim}{\boldsymbol{\sigma}}^b$ and the stress state is found to be homogeneous in the tensile specimen.

3.1.2. *Plastic strain state*

In an isotropic material undergoing simple tension in the direction y, the plastic strain states in the sample in the areas (a) and (b) take the form:

$$\left[\underset{\sim}{\boldsymbol{\varepsilon}}^p_a\right] = \begin{bmatrix} -\frac{\varepsilon^p_a}{2} & 0 & 0 \\ 0 & \varepsilon^p_a & 0 \\ 0 & 0 & -\frac{\varepsilon^p_a}{2} \end{bmatrix}; \quad \left[\underset{\sim}{\boldsymbol{\varepsilon}}^p_b\right] = \begin{bmatrix} -\frac{\varepsilon^p_b}{2} & 0 & 0 \\ 0 & \varepsilon^p_b & 0 \\ 0 & 0 & -\frac{\varepsilon^p_b}{2} \end{bmatrix} \tag{4}$$

The total strain jump at the (a)/(b) interface must fulfill the Hadamard compatibility conditions [30]. Since the stress state has been shown to be homogeneous, the total strain jump coincides with the plastic strain jump at the interface. It has the form:

$$[\![\underset{\sim}{\boldsymbol{\varepsilon}}^p]\!] = \frac{1}{2}\left(\underline{\boldsymbol{g}} \otimes \underline{\boldsymbol{n}} + \underline{\boldsymbol{n}} \otimes \underline{\boldsymbol{g}}\right) \tag{5}$$

where $\underline{\boldsymbol{g}}$ is the intensity of the plastic strain discontinuity to be determined. Equations (4) and (5) lead to:

$$\left(\varepsilon^p_b - \varepsilon^p_a\right)\begin{bmatrix} -\frac{1}{2} & 0 & 0 \\ 0 & 1 & 0 \\ 0 & 0 & -\frac{1}{2} \end{bmatrix} = \begin{bmatrix} -g_1\sin\theta & \frac{g_1\cos\theta - g_2\sin\theta}{2} & 0 \\ \frac{g_1\cos\theta - g_2\sin\theta}{2} & g_2\cos\theta & 0 \\ 0 & 0 & 0 \end{bmatrix} \tag{6}$$

As a result of (6), a strain discontinuity is possible if the angle between the band normal and the vertical axis takes the following value:

$$\tan^2\theta = \frac{1}{2}; \quad \frac{\pi}{2} - \theta = 54.7^\circ \tag{7}$$

3.2. *Constitutive equations*

The main macroscopic features of the Lüders phenomenon can be simulated using the finite element method. In references [19] and [9] the chosen constitutive equations rely on a linear softening branch followed by a linear hardening branch in the

Table 4. Parameters for the phenomenological plasticity model of Section 3.2.

R_0 (MPa)	Q_1 (MPa)	b_1	Q_2 (MPa)	b_2	Q_3 (MPa)	b_3
325	325	12	−60	200	20	2000

work-hardening material function. In the case of the tension of a plate, the initial softening part induces strain localization inside a band and the subsequent hardening behavior leads to the propagation of the band front until the whole plate is filled. The same paradigmatic idea is used in the present work, but nonlinear local behavior is introduced here in the form of exponential hardening functions with the objective of having smooth and differentiable hardening functions. The yield stress for a given amount of accumulative plastic strain p is called $R(p)$:

$$R(p) = R_0 + Q_1\left(1 - e^{-b_1 p}\right) + Q_2\left(1 - e^{-b_2 p}\right) + Q_3\left(1 - e^{-b_3 p}\right) \tag{8}$$

where R_0 is the initial yield strength, and Q_1, Q_2, Q_3, b_1, b_2 and b_3 are material parameters with $Q_1, Q_3 > 0$ and $Q_2 < 0$. The corresponding values of the parameters are given in Table 4. A Voce classic strain hardening behavior is introduced in the first part of the equation [31]. An additional softening term is added with a negative coefficient Q_2 to model in a purely phenomenological way static strain aging. The third additional hardening is used to round off the first peak in the local law and provide a better convergence in the finite element calculations. For the elastic behavior the Young's modulus is 210 GPa and Poisson's ratio is 0.3. The resulting local behavior is plotted in Figure 7a. The dislocations are initially locked by solute carbon and nitrogen atoms, and the increase in yield strength represents the stress that has to be overcome to unlock or multiply these dislocations. Once this threshold is overcome, a rapid multiplication of mobile dislocations occurs, which is represented by the decrease of the yield stress. This softening behavior leads to plastic strain localization. After the propagation of the band throughout the specimen, homogeneous hardening takes place.

3.3. *Numerical results: evidence of mesh dependency*

Two-dimensional simulations were carried out using the finite element code *Zset* [32]. The global size of the considered dogbone tensile specimen under plane stress conditions is 64 mm length and 14 mm width. The gauge length area has 36 mm length and 6 mm width. Various types of meshes are presented in Figure 6, including different element shapes and mesh refinement. We give them the following names:

- *Regular mesh*: square elements with two levels of refinement; the mesh size is equal to 0.5 mm in Figure 6a and to 0.25 mm in Figure 6b.
- *Random mesh*: randomly distributed triangular elements as shown in Figure 6c.
- *Oriented mesh*: two levels of refinement for oriented triangular elements, see Figure 6d and e; the rows of triangular elements are oriented along lines at an angle of 54.7° with respect to the tensile direction,

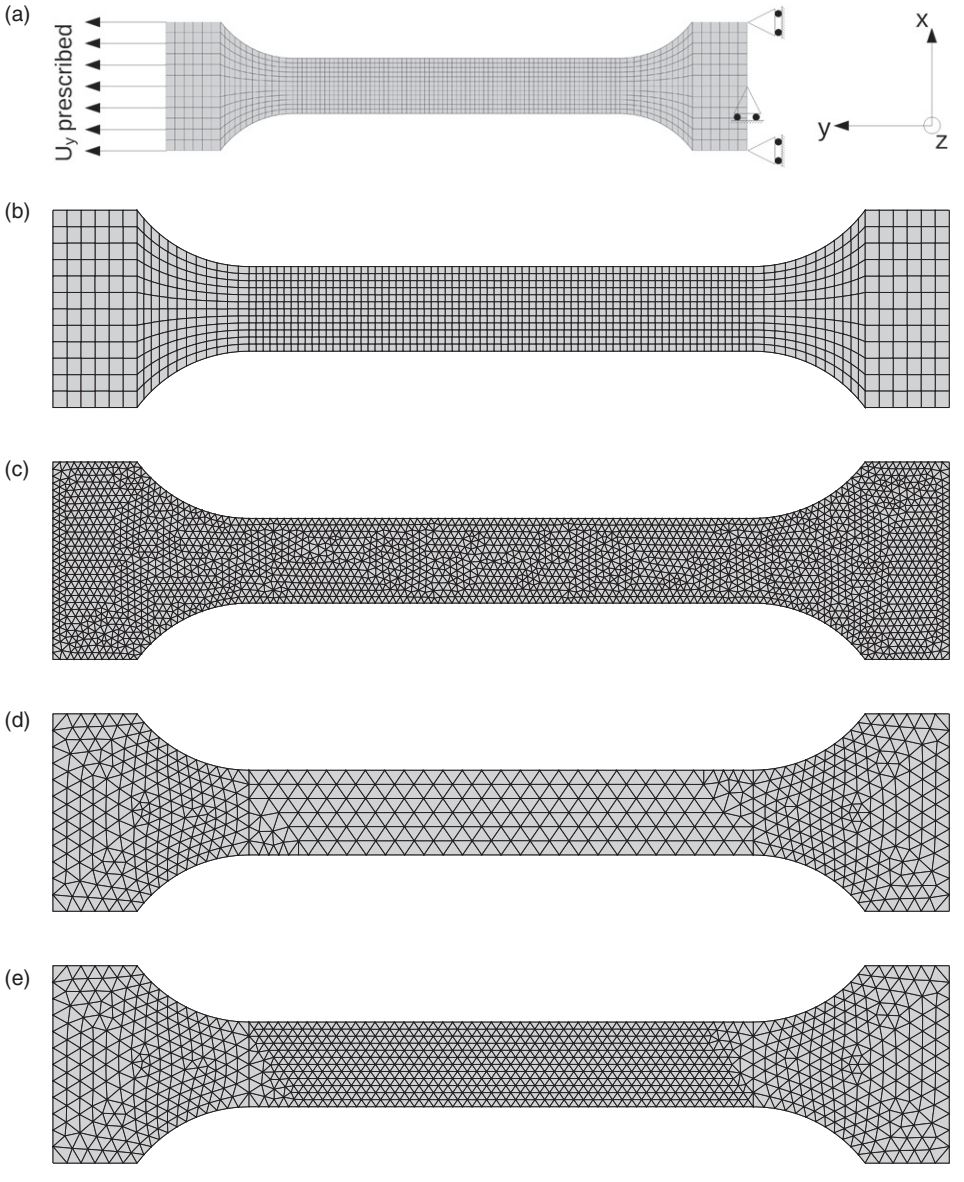

Figure 6. Different meshes tested and boundary conditions: (a) boundary conditions, (b) regular (13442 DOF), (c) random (30792 DOF), (d) oriented (8024 DOF) and (e) fine oriented (14248 DOF).

following Equation (7). As a result, the Lüders bands will be parallel to element edges. This configuration naturally allows strain jumps along the element edges and leads to a proper description of strain discontinuities.

For each mesh, the number of degrees of freedom (DOF) is given in the caption of Figure 6. The boundary conditions are indicated in Figure 6a. The load consists of a

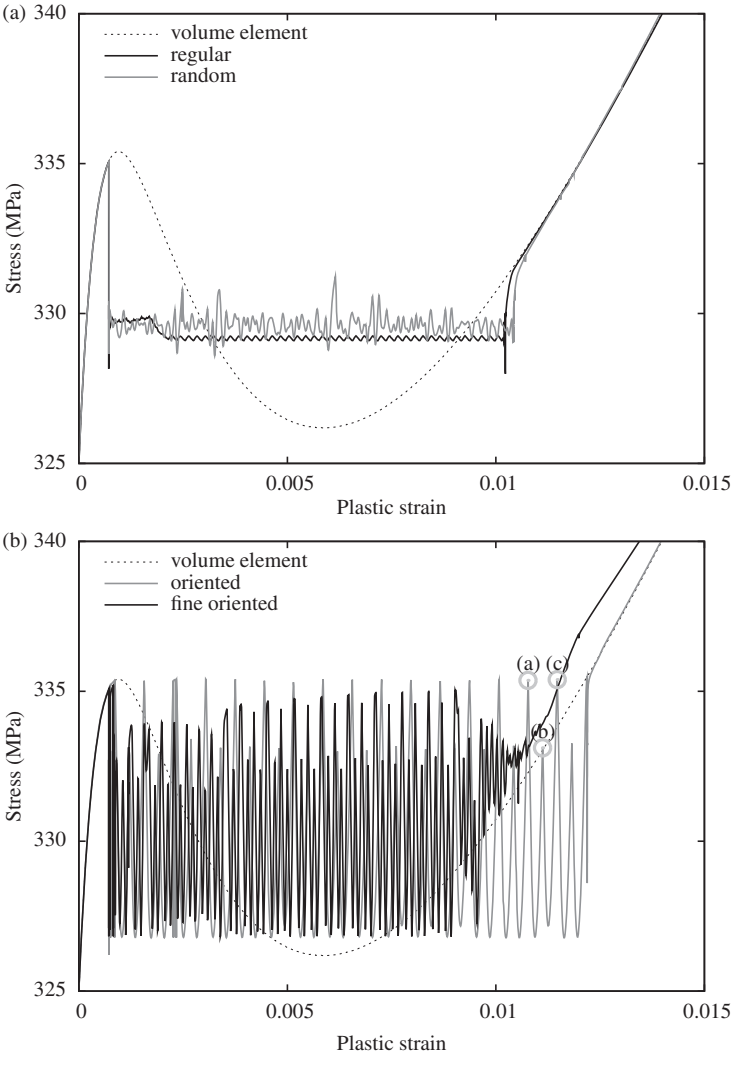

Figure 7. Overall curves from the finite element solutions of a tensile test with a standard plasticity model for different mesh types and the same material parameters: (a) regular and random meshes, (b) oriented meshes. The overall strain rate is constant and equal to $10^{-4}\,s^{-1}$.

head displacement of 1 mm along the vertical axis. Simulations have been carried out under plane stress conditions with the small deformation hypothesis. All the elements have quadratic shape functions and reduced Gauss integration.

Figure 7 shows the resulting curves, namely the overall stress (F/S_0) as a function of an overall plastic strain defined as follows. The total strain is calculated using a numerical extensometer, i.e. it is defined as the ratio of the relative displacement of two points along a vertical line, divided by the initial distance between them. The elastic strain is subtracted from the global strain to obtain an overall plastic strain. As experimentally observed, the macroscopic behavior exhibits a plateau whose

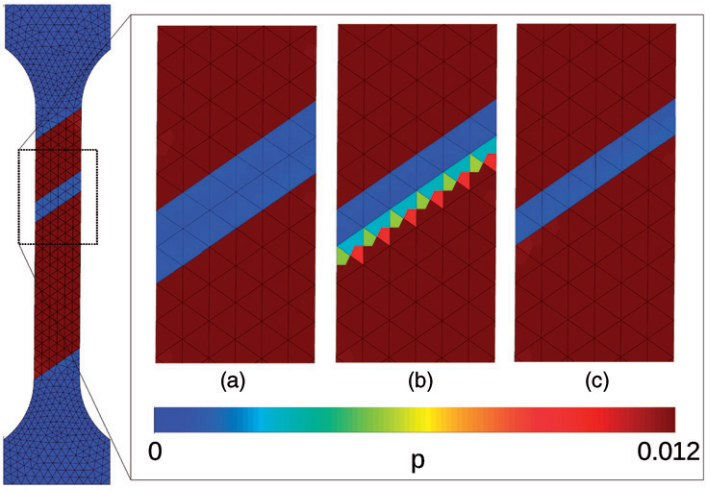

Figure 8. Lüders band propagation for the oriented mesh of Figure 6d. The color scale indicates the level of the plastic strain.

length is called the Lüders strain. The plateau displays oscillations which are found to depend on the mesh type. The strongest oscillations are found in the case of the oriented meshes which give a proper description of the strain discontinuity at the front of the Lüders band.

The kinematics of the band propagation for the oriented mesh is shown in Figure 8. The accumulative plastic strain field is given at three particular steps (a), (b) and (c) indicated on the overall loading curve of Figure 7b. Two bands propagate in the sample but they move forward successively. The plastic strain inside the band is $\varepsilon_p \approx 0.012$ which is in agreement with the Lüders strain obtained from the overall loading curve, $\varepsilon_L \approx 0.012$. Each oscillation corresponds to the plastification of one row of elements. When plastic straining starts ahead of the Lüders band front, the stress drops to a minimal value and then increases again towards the maximal value, following the constitutive law (8). At that latter point, the next row of elements is plastically activated. This scenario explains the huge oscillations in Figure 7b.

The strain profile shown in Figure 9 corresponds to the iso-plastic strain map of Figure 8a. The head band front is stopped when the foot band front propagates. The level of Lüders strain is the same as evaluated from Figures 7b and 8. The profile strain of the Lüders band is a square pulse, with a clear discontinuity, as modeled in [33].

4. Strain gradient plasticity model

4.1. *Motivation*

The numerical results in Section 3.3 reveal a strong mesh dependency of the plateau regime of the overall loading curves. Oscillations of various amplitudes are obtained that culminate in the case of element edges parallel to the front band.

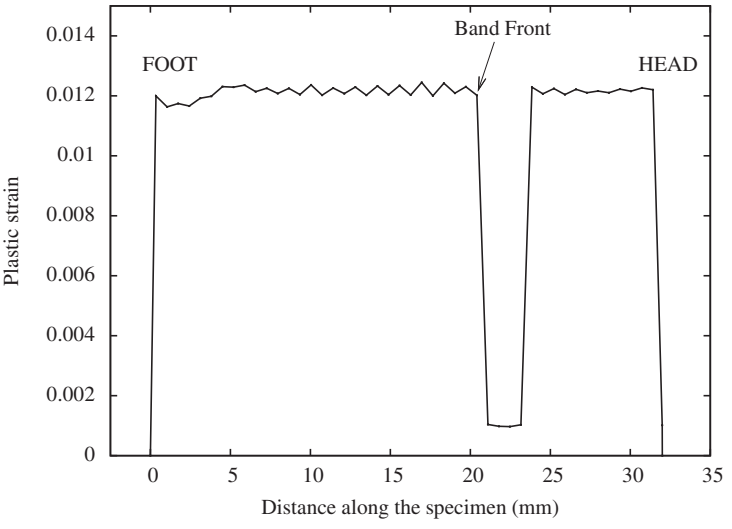

Figure 9. Plastic strain along the specimen's vertical axis. This graph is deduced from the iso-strain map of Figure 8a.

Such oscillations prevent us from determining a precise value for the plateau stress. On the other hand, the standard model predicts a sharp transition from the Lüders band to the plastically undeformed zone, see Figure 9. This in contradiction with strain field measurements indicating the existence of a smooth front band zone. A smooth front band whose width can be controlled by specific material parameters is needed.

Both numerical and physical limitations can be solved by resorting to a strain gradient plasticity model as recommended in [22,27,28] for the simulation of the Lüders phenomenon. Strain gradient plasticity can be regarded as a mathematical regularization method that restores the well-posedness of the boundary value problem in the presence of strain-softening effects [26]. On the other hand, it introduces an intrinsic length in the mechanical model which reflects some aspects of the underlying microstructure of the material, here related to the cooperative deformation of grains of given size in a polycrystal. The "Aifantis"-type Laplace term is introduced in this work in a purely phenomenological way to suppress the spurious mesh dependence observed with the standard model. However, there exist more fundamental motivations related to the diffusive character of dislocation motion and the induced dislocation structure formation, as discussed in reference [22] for dynamic strain aging and in reference [29] for Lüders band propagation in polycrystals. Nevertheless, we are not in a position here to justify the characteristic size of the Lüders band front from microstructural considerations.

The strain gradient plasticity model considered in the present work belongs to the class of so-called micromorphic theories presented in [26]. It has the advantage that its implementation in a finite element program is rather straightforward and that, with a convenient choice of material parameters, it reduces to the well-known Aifantis strain gradient plasticity model.

4.2. *Theory*

The classical non-regularized model describes an elastoplastic material behavior characterized by the tensor of elastic moduli $\underset{\approx}{\underset{\approx}{\boldsymbol{\Lambda}}}$ and the nonlinear hardening variable R. In the micromorphic extension of this classical model, a new degree of freedom, p_χ, is introduced which has the physical meaning of a plastic microdeformation (see [26] for a more detailed presentation of the model). It has to be compared to the accumulative plastic strain p. Under homogeneous loading conditions, we have $p_\chi = p$, whereas the plastic microdeformation can differ from p in the presence of strong strain gradients. Two additional material parameters are introduced, namely, the coupling modulus H_χ (unit MPa) and the micromorphic higher order modulus $\underset{\approx}{\boldsymbol{A}}$ (unit MPa m^2).

$$\underset{\approx}{\boldsymbol{\sigma}} = \underset{\approx}{\underset{\approx}{\boldsymbol{\Lambda}}} : \underset{\approx}{\boldsymbol{\varepsilon}}^e \tag{9}$$

$$a = -H_\chi(p - p_\chi) \tag{10}$$

$$\underline{\boldsymbol{b}} = \underset{\approx}{\boldsymbol{A}} \cdot \nabla p_\chi \tag{11}$$

$$R = R(p) + H_\chi(p - p_\chi) \tag{12}$$

where a and $\underline{\boldsymbol{b}}$ represent generalized stresses conjugate to the plastic microdeformation and its gradient, respectively, in the generalized work of internal forces. The classical and generalized stress tensors must fulfill two balance equations in the form of divergence equations:

$$\operatorname{div} \underset{\approx}{\boldsymbol{\sigma}} = 0, \quad \operatorname{div} \underline{\boldsymbol{b}} - a = 0 \tag{13}$$

in the absence of body forces and in the static case.

When inserted in the additional balance, the state laws lead to the following partial differential equation:

$$p_\chi - \frac{1}{H_\chi} \operatorname{div}(\underset{\approx}{\boldsymbol{A}} \cdot \nabla p_\chi) = p \tag{14}$$

Let us specialize this equation to the case of isotropic materials, for which the second order tensor of micromorphic stiffness reduces to $\underset{\approx}{\boldsymbol{A}} = A\underset{\approx}{\boldsymbol{I}}$ which involves a single additional material parameter. Equation (14) then becomes:

$$p_\chi - l_c^2 \Delta p_\chi = p, \quad \text{with} \quad l_c^2 = \frac{A}{H_\chi} \tag{15}$$

where l_c is the characteristic length of the model.

As a result, the hardening function can also be written:

$$R = R(p) - A\Delta p_\chi \tag{16}$$

The material parameter H_χ can also be seen as a penalty coefficient that forces the relative plastic strain $e = p - p_\chi$ to remain small. It can be shown that a high value of

H_χ keeps e close to zero. In that case, the plastic microdeformation p_χ in the hardening law (16) can be replaced by p itself:

$$R = R(p) - A\Delta p \tag{17}$$

which is exactly the Aifantis strain gradient plasticity model, see [34]. In that case, there is one single new material parameter, namely l_c.

4.3. *Regularization*

The same meshes and database as in Section 3.3 have been used in order to validate the regularization power of the model. In Figure 10, the macroscopic stress-plastic strain curves with the meshes of Figure 6 are plotted. The large oscillations have disappeared for the oriented meshes. All types of meshes converge toward a unique solution with the same plateau level, provided a sufficient number of elements is used.

In the same way as in Section 3.3, the evolution of plastic strain is plotted in Figure 11. This evolution is much more diffuse than in the absence of regularization. In particular the strong discontinuity observed with the classical model is replaced by a smooth transition from the Lüders band to the plastically undeformed domain. This tendency is confirmed with the observation of the plastic strain along the specimen's vertical axis shown in Figure 12. The shape of the plastic distribution is similar to the one found in the theoretical analysis [35].

The characteristic length l_c was chosen equal to 3.16 mm, with $A = 10^5$ MPa mm^2 and $H_\chi = 10^4$ MPa. Other simulations were carried out with different characteristic lengths and the plateau level has been found to be independent of the

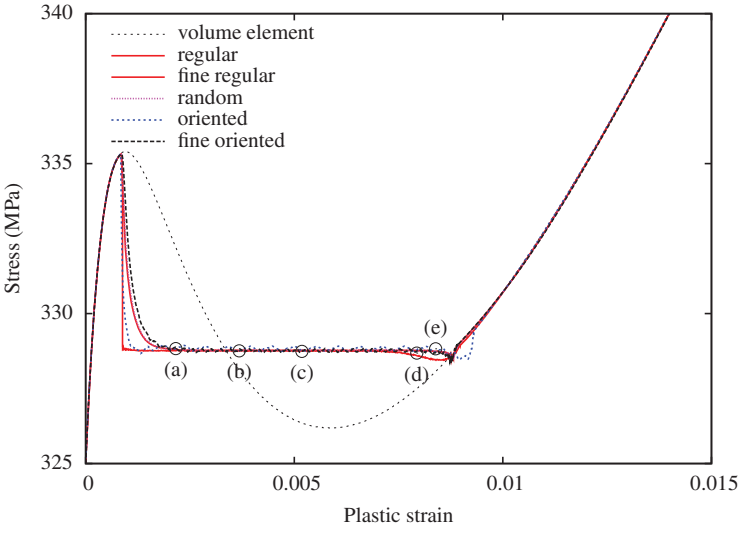

Figure 10. Overall curves obtained from finite element simulations of a tensile test with the microplasticity model for each mesh type and the same material parameters. The strain rate is constant and equal to 10^{-4} s^{-1}, $l_c = 3.16$ mm.

characteristic length at least if the element size remains small compared to l_c. The characteristic length was found to control the front band width. Convergence with respect to mesh discretization is reached when the element size in the front band zone is at least five times smaller than the characteristic length l_c.

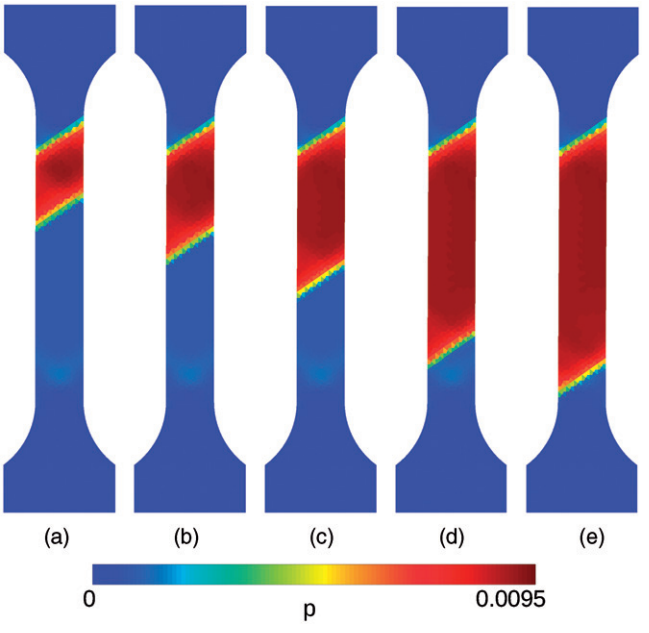

Figure 11. Lüders band propagation in the oriented mesh of Figure 6d with the microplasticity model. Field of accumulative plastic strain.

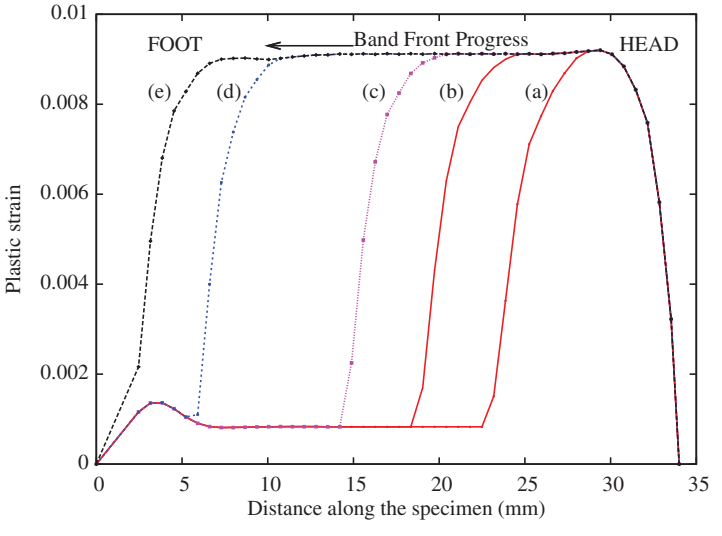

Figure 12. Plastic strain along the specimen's vertical axis. This graph is deduced from the iso-strain map of Figure 11.

The additional material parameter A and the corresponding characteristic length l_c were chosen in such a way that the computed front band width is in agreement with the front band width found in the strain field measurements of Section 2.3.

5. Identification of the material parameters of the static strain-aging model

The simulation of strain aging requires a suitable choice of an elastoviscoplastic model based on strain-aging physical mechanisms of pinning and unpinning of dislocations. The previous elastoplastic model with softening is not sufficient to account for several Lüders effects like prestraining followed by thermal aging. The model retained in this work and initially proposed by McCormick [20,21] is based on an internal variable t_a called the aging time. It has been implemented in the finite element code *Zset* [23,26,36]. The numerical local integration of the constitutive equations is performed using a mixed approach between classical Runge–Kutta and implicit Newton methods. This original method allows us to limit local divergences and provides an evaluation of the consistent tangent matrix for the global implicit resolution of the finite element scheme.

The strain rate tensor $\dot{\underset{\sim}{\varepsilon}}$ is split into elastic and plastic contributions, the evolution of the latter being given by the plastic flow rule. The stress is computed from the elastic strain $\underset{\sim}{\varepsilon}_e$ through Hooke's law:

$$\dot{\underset{\sim}{\varepsilon}} = \dot{\underset{\sim}{\varepsilon}}_e + \dot{\underset{\sim}{\varepsilon}}_p, \quad \underset{\sim}{\sigma} = \underset{\approx}{\Lambda} : \underset{\sim}{\varepsilon}_e \tag{18}$$

The plastic strain is computed from the normality law rule and the equivalent plastic strain rate $\dot{p}$ follows a thermal activation law defined as:

$$\dot{\underset{\sim}{\varepsilon}}_p = \dot{p}\underset{\sim}{n}, \quad \underset{\sim}{n} = \frac{\partial f}{\partial \underset{\sim}{\sigma}} = \frac{3}{2}\frac{\underset{\sim}{s}}{J_2(\underset{\sim}{\sigma})} \tag{19}$$

$$\dot{p} = \dot{p}_0 \sinh\left(\frac{f}{K}\right) = \dot{\varepsilon}_0 \exp\left(-\frac{E_a}{k_B T}\right) \sinh\left(\frac{V_a \langle f(\underset{\sim}{\sigma}, \rho, t_a)\rangle}{k_B T}\right) \tag{20}$$

where T is the temperature in kelvin, k_B is Boltzmann's constant and $\dot{\varepsilon}_0$, E_a and V_a are respectively a strain rate parameter, the activation energy and the activation volume of the physical mechanisms of plasticity.

The function f is the yield function which is based on a von Mises criterion with isotropic hardening:

$$f(\underset{\sim}{\sigma}, \rho, t_a) = J_2(\underset{\sim}{\sigma}) - R(\rho) - R_a(t_a) \tag{21}$$

$$R(\rho) = \sigma_0 + \gamma\mu b\sqrt{\rho}, \quad \dot{\rho} = A\left(1 - \frac{\rho}{B}\right)\dot{p}, \quad R_0 = \sigma_0 + \gamma\mu b\sqrt{\rho_0} \tag{22}$$

where $J_2(\underset{\sim}{\sigma})$ is the von Mises invariant of the stress tensor. The dislocation density ρ is introduced in the model (initial value ρ_0). The classical strain hardening is given by the term $R(\rho)$ which follows the evolution law defined in Equation (22), the parameters characterizing the evolution law of this variable being A and B.

The dislocation density evolution rule is driven by the cumulative plastic strain rate $\dot{p}$, as done for instance in [24]. The yield stress R_0 is the initial "microscopic yield stress," corresponding to the yield stress that would be measured in the same steel in the absence of static strain aging.

The second hardening term, $R_a(t_a)$, is induced by strain aging, following [23,37,38]. It depends on a new internal variable t_a called the aging time. It takes the form:

$$R_a(t_a) = P_1 C_s(t_a), \quad \text{with} \quad C_s = 1 - \exp\left[-\left(\frac{t_a}{t_0}\right)^n\right] \tag{23}$$

$$\dot{t}_a = 1 - \frac{t_a \dot{p}}{\omega} \tag{24}$$

The strain-aging term R_a is proportional to the variable C_s that is related to the over-concentration of solute atoms around pinned dislocations. This variable increases with the aging time t_a, the totally pinned state being given by $C_s = 1$. The unpinned state corresponds to $C_s = 0$. The parameter P_1 corresponds to the maximal additional stress needed to switch between pinned and unpinned states. The parameter t_0 and the power n control the kinetics of the pinning process. Another parameter labeled ω appears in the evolution law of the aging time. It is related to the incremental strain resulting from the jump of unpinned dislocations.

5.1. *Identification procedure at the material point level*

Classically in tensile tests, the experimental results are obtained on specimens in which the mechanical fields are homogeneous in most of their gauge length, so that the specimen can be considered as a volume element. The parameters are identified from the comparison between experimental and simulation results based on standard optimization procedures. However, the identification procedure of a strain-aging model from experimental data significantly differs from the usual identification approach. This is due to the fact that some model parameters are related to the strain localization patterns that develop on the specimen surface and to the corresponding peak and plateau on the tensile curve. That is why many finite element simulations on full specimens were necessary in [39] for the identification of the complete strain-aging model over a large range of temperature. These costly finite element simulations lead to a long and difficult identification process. In the case of Lüders behavior, we show in the present work that the identification procedure can be limited to material point evaluations. The new identification procedure is then decomposed into two main steps:

- Optimization: volume element simulations are carried out for the identification of all parameters. The originality in this work is to identify the 12 parameters of the model, accounting for strain hardening, viscosity and aging, from volume element simulations.
- Validation: finite element simulations on a 2D tensile sample under plane stress conditions are carried out to validate the optimization. The objective of the identification at this stage is to obtain the correct orientation of the

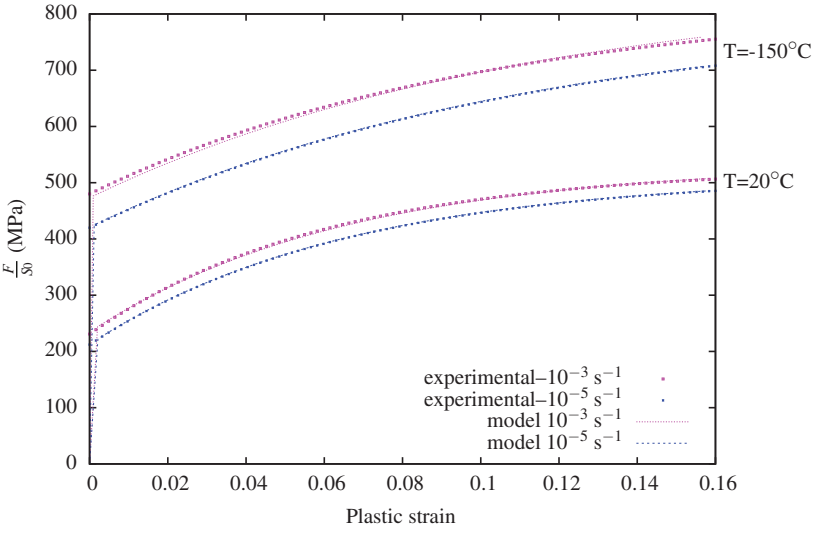

Figure 13. Identification for 20 and −150°C at 10^{-3} and $10^{-5}\,s^{-1}$.

Lüders band and to validate the correlation between experimental and numerical strain–stress tensile curves.

5.2. *Hardening and viscosity*

First of all, the hardening and viscosity parameters are identified. In this first step, the Lüders peak and the Lüders strain are not taken into account. The parameters are determined from 20 to −150°C from the tensile curves at two strain rates, 10^{-3} and $10^{-5}\,s^{-1}$ (see Figure 13). The following notations are introduced:

$$\dot{p}_0(T) = \dot{\varepsilon}_0 \exp\left(-\frac{E_a}{k_B T}\right) \tag{25}$$

$$K(T) = \frac{k_B T}{V_a} \tag{26}$$

The viscoplastic parameters are identified by tensile tests at different strain rates. The value of the activation energy is equal to 0.6 eV as it should be [24]. The value of $\dot{\varepsilon_0}$ is chosen in order to get always a positive strain rate sensitivity as observed in the investigated temperature and strain rate range.

The parameters A, B and σ_0 are also fitted using experimental curves from which the peak and lower yield point are excluded. Table 5 shows the optimized parameters. The Burgers vector is equal to 0.228 nm [39] and the initial dislocation density, ρ_0, is equal to $10^{13}\,m^{-2}$ [36]. Note that the values of A and B are rather high. Between 0 and 16% of plastic strain, at room temperature, there is approximately 300 MPa of hardening. The dislocation density equivalent at 16% of plastic strain

Table 5. Model parameters for viscosity, hardening and elasticity.

T (°C)	−150	−100	−50	0	20
E (GPa)	214	220	219	221	218
ν	0.3	0.3	0.3	0.3	0.3
R_0 (MPa)	170	147	107	130	136
σ_0 (MPa)	150	127	87	110	116
A (m^{-2})	$2.256 \times 10^{+16}$	$3.503 \times 10^{+16}$	$4.149 \times 10^{+16}$	$3.873 \times 10^{+16}$	$3.086 \times 10^{+16}$
B (m^{-2})	$1.474 \times 10^{+16}$	$9.204 \times 10^{+15}$	$8.082 \times 10^{+15}$	$5.118 \times 10^{+15}$	$5.115 \times 10^{+15}$
$\dot{\varepsilon}_0$ (s^{-1})	6.2	6.2	6.2	6.2	6.2
E_a (eV)	0.6	0.6	0.6	0.6	0.6
V_a (b^3)	27	59	90	121	133

must be around $2.5 \times 10^{15}\,m^{-2}$. The chosen values of the parameter A and B are compatible with such a hardening and such dislocation densities. This dislocation density is probably too high and has not been checked by TEM observations. The necessity of such values for calibrating the model suggests that our hypothesis of almost total unpinning after the Lüders peak is probably exaggerated and is compensated for by too much hardening in our model. Additional elaborate experiments will be required to estimate the unpinning ratio in the Lüders phenomenon.

5.3. *Aging*

After the previous step, the parameters which govern the aging contribution are calibrated. The identification of parameters P_1, t_0 and n is explained first. The strain-aging hardening contribution R_a is controlled by: P_1, t_0, n, ω and by the initial aging time t_{a0}. The value of ω essentially influences the localization pattern in the 3D simulation [36]. This parameter ω is kept constant here and equal to 5×10^{-4}, after [36].

5.3.1. *Parameter t_0 and initial condition t_{a0}*

The existence of aging prior to deformation is modeled by means of a non-vanishing initial value t_{a0} of the internal variable t_a. The characteristic time t_0 then controls the relaxation of the concentration $C_s(t_a)$ from its initial value $C_s(t_{a0})$, which corresponds to the unpinning stage in the Lüders phenomenon. Figure 14 illustrates the relaxation profiles depending on the ratio t_{a0}/t_0. When $t_{a0} > t_0$, the profile is rather flat at the beginning of plastic flow so that, in the finite element simulation, strain localization will be postponed. A suitable description of the peak stress therefore requires $t_{a0} \leq t_0$. In this work, we take $t_{a0} = t_0$, so that there is a fixed point at $p = 0$. The main advantage of choosing $t_{a0} = t_0$ is that C_s remains constant and equal to 0.63 when $p = 0$ for any value of the parameter n. t_0 is fitted to control the unpinning level which is represented at the bottom of Figure 15. The t_0 value must be such as to minimize the pinning level when $p \to +\infty$.

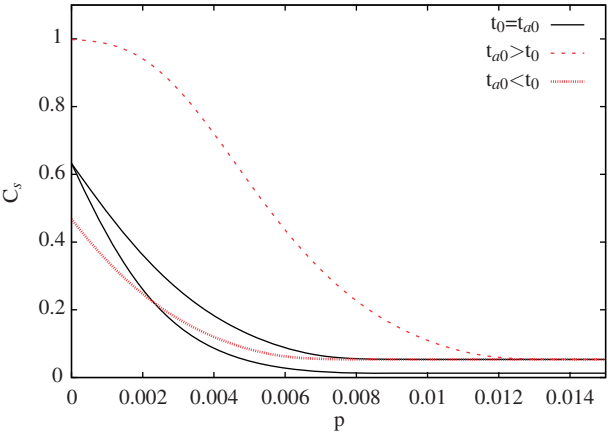

Figure 14. Profiles of C_s as a function of p during a tensile test depending on the initial value t_{a0} compared to material parameter t_0.

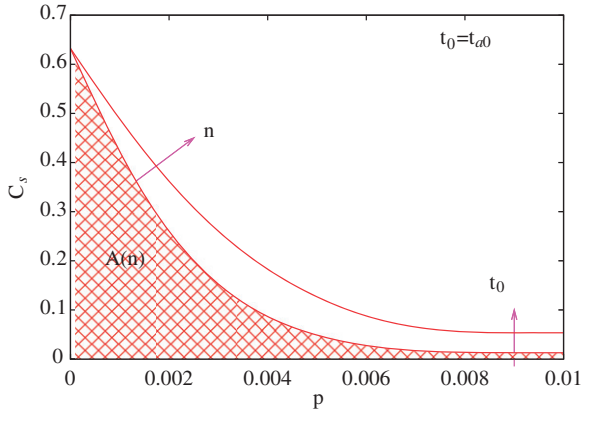

Figure 15. Evolution of the aging contribution $R_a(p)/P_1$ as a function of plastic strain and the role of the parameters t_0 and n.

5.3.2. *Parameter P_1*

The parameter P_1 controls the contribution of the pinning process on the flow stress. It can be interpreted as the interaction force between mobile dislocations and solute atoms. The amplitude of the Lüders peak stress is directly related to the value of P_1. Figure 16 illustrates the procedure to determine P_1 from $R_{a0} = R_a(0) = 0.63P_1$. The value of R_{a0} can be directly identified from the peak stress and the initial yield stress R_0 in the absence of aging. The value of P_1 follows.

5.3.3. *Parameter n*

The parameter n controls the hatched area in the relaxation of C_s, as shown in Figure 15. This parameter is calibrated in order to fulfill Maxwell's equal area rule.

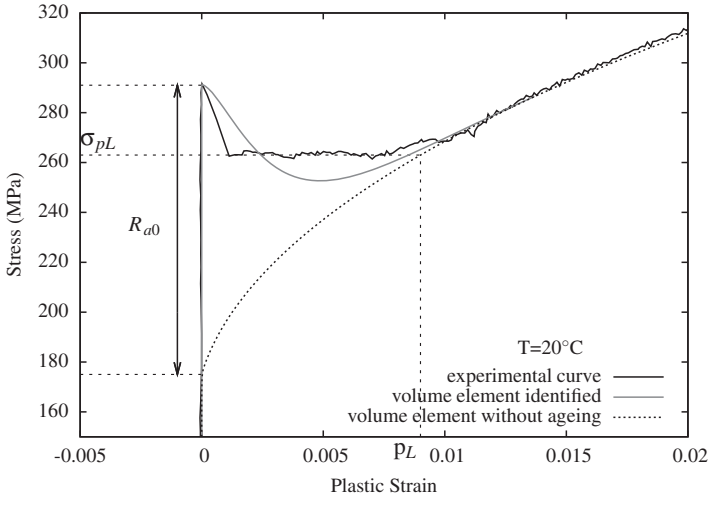

Figure 16. Determination of parameter P_1 from the experimental curve including the peak stress.

Table 6. Model parameters for aging.

T (°C)	−150	−100	−50	0	20
P_1 (MPa)	381	304	282	221	183.2
t_0 (s)	3.49×10^{13}	1.24×10^{12}	2.81×10^{8}	1.01×10^{5}	1.59×10^{4}
t_{a0} (s)	3.49×10^{13}	1.24×10^{12}	2.81×10^{8}	1.01×10^{5}	1.59×10^{4}
ω	5×10^{-4}	5×10^{-4}	5×10^{-4}	5×10^{-4}	5×10^{-4}
n	0.137	0.144	0.199	0.306	0.334

According to this rule, the plastic dissipation between $p = 0$ and $p = p_L$, formed by the area $A(n)$ multiplied by P_1 in Figure 15, must be equal to the experimental area below the plateau. This area multiplied by P_1 is equal to the product of the plateau stress σ_{pL} and the Lüders strain p_L. It is recalled that the Lüders strain is the intersection between the plateau and the hardening curve without aging (material point without aging) in Figure 16.

Table 6 shows the optimized aging parameters for all temperatures.

5.4. *Validation by means of 2D finite element simulations*

The previous identification strategy has the advantage that it does not require any finite element simulation on the whole sample. The localization is taken into account by considering the peak stress and the existence of Maxwell's rule for the dissipated energy, but the simulations are limited to material point evaluations. This is in contrast to existing identification procedures for such models, for instance in [39].

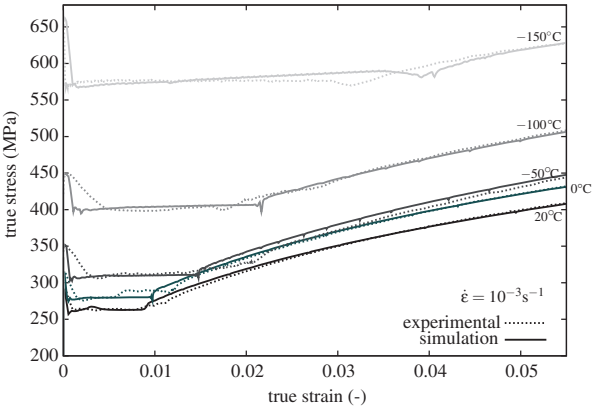

Figure 17. Comparison between experimental and simulation curves for all the temperatures at the strain rate $10^{-3}\,\text{s}^{-1}$.

However, finite element simulations are necessary to validate the ability of the model to capture the main features of the strain localization phenomena. The first validation is performed by means of 2D finite element simulation of Lüders band formation and propagation. The predicted overall load–displacement curves for the tensile tests can be compared to the experimental ones. It includes the peak height, the plateau level and the Lüders strain. These results are given in Figure 17 which shows the simulated and experimental tensile curves at $\dot{\varepsilon} = 10^{-3}\,\text{s}^{-1}$ for various temperatures. The predicted Lüders peak height and the plateau level are in good agreement with the experimental ones. The Lüders strain is almost identical to the experimental plateau length.

5.5. *Validation on 3D samples*

It is well-known that the strain localization phenomena can be quite different in 2D and 3D because plane stress conditions are more prone to localization [40]. That is why the final validation is performed on the real 3D specimen geometry. Attention is focused on the formation of an inclined Lüders band with the proper orientation as observed experimentally in Section 2.3. The geometry of the specimen is the same as the experimental one in Figure 1. The boundary conditions are shown in Figure 18a. Figure 19 shows the evolution of cumulative plastic strain at the strain rate of $10^{-3}\,\text{s}^{-1}$ with the boundary conditions (a). The band front is found to be rather horizontal which is in contradiction to the theoretically and experimentally expected orientation.

In fact, the simulated band orientation strongly depends on the strain rate. For, the simulation at the strain rate of $10^{-7}\,\text{s}^{-1}$ with the same boundary conditions leads to a properly inclined band. Simulations at higher strains lead to conical bands with a horizontal intersection with the outer surface of the specimen, in contrast to the experimental results. In a cylindrical specimen, all inclined bands making an angle of 55° with respect to the tensile axis are theoretically allowed strain localization modes.

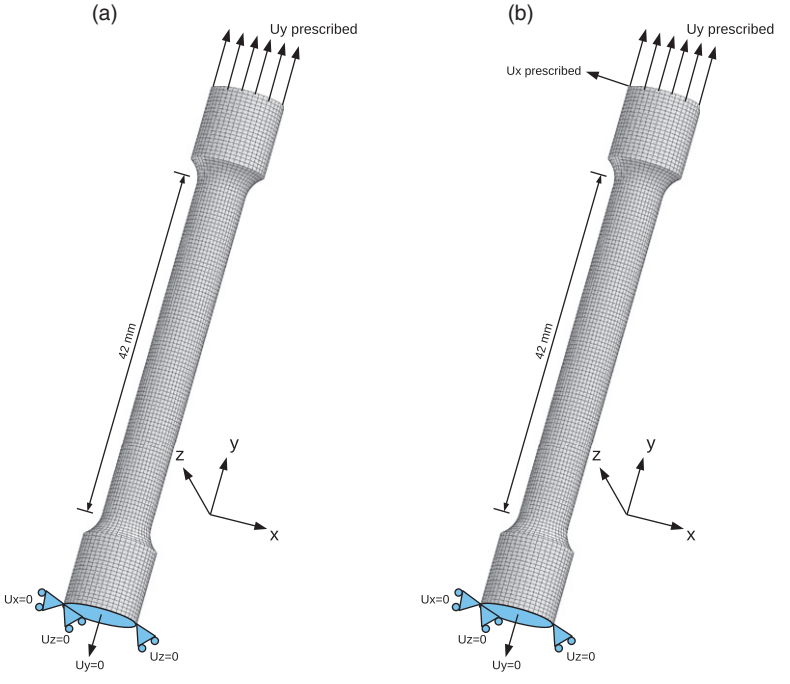

Figure 18. 3D mesh and boundary conditions. (a) Prescribed vertical displacement; (b) superimposed vertical and horizontal prescribed displacements.

In the finite element simulation, all of them can occur with the same probability. When they all form simultaneously, a conical localization zone is obtained as in Figure 19. Any perturbation can lead to a symmetry-breaking mode made of a single inclined band as discussed in the next paragraph. If the material is highly unstable, a numerical perturbation which is inevitable in computational mechanics, is sufficient to induce such symmetry breaking. However, viscosity can stabilize the cone-shaped mode. Currently, there is no theoretical tool that can tell us from the values of the material parameters including viscosity, whether a symmetry-breaking or a cone-shaped mode will occur. To check it, the full finite element perturbation must be performed. Several localization criteria are available, as discussed in [41], but, in their present form, they cannot be used to predict which possible localization mode will finally occur in the simulation. This is an incentive for future research on the imperfection sensitivity of strain localization phenomena in elastoviscoplasticity.

To trigger inclined Lüders bands at higher strain rates, we have found that a perturbation to the previous boundary conditions must be introduced, as shown in Figure 18b. The loading condition consists of a head displacement of 6.72 mm along the vertical axis. The strain rate is equal to $10^{-3}\,s^{-1}$. A small horizontal head displacement of 100 μm is also prescribed which corresponds to 1.5% of the vertical displacement. Such small perturbations are expected to occur in the mechanical testing system. The propagation of the Lüders band can be seen in Figure 20.

Figure 19. Evolution of cumulative plastic strain at the strain rate $10^{-3}\,s^{-1}$ with the boundary conditions of Figure 18a. View of the outer surface (left), 3/4 of the specimen (middle), and one half of the specimen (right).

It started from one grip of the specimen. The orientation of the front band is determined by visualizing the plastic strain rate.

The profiles of plastic strain along a vertical line on the outer surface of the specimen are given in Figure 21 at different stages of the progress of the Lüders band. A smooth band front is observed on all profiles. A bump is observed at the lower part of the band, probably due to the formation of overlapping bands coming from the grip zone of the specimen. Such bumps are reminiscent of the oscillations observed on the experimental profiles of Figure 4.

6. Conclusion and outlook

An original identification procedure has been proposed to determine the material parameters of a constitutive elastoviscoplastic model accounting for Lüders effects in a C-Mn steel over a large temperature range. The model has been calibrated from the knowledge of the peak stress, plateau stress, Lüders strain and from the extrapolation of the intrinsic hardening behavior. It is based on a modified Estrin–Kubin–McCormick model [42]. This identification method enables separated calibration of viscosity, hardening and aging parameters.

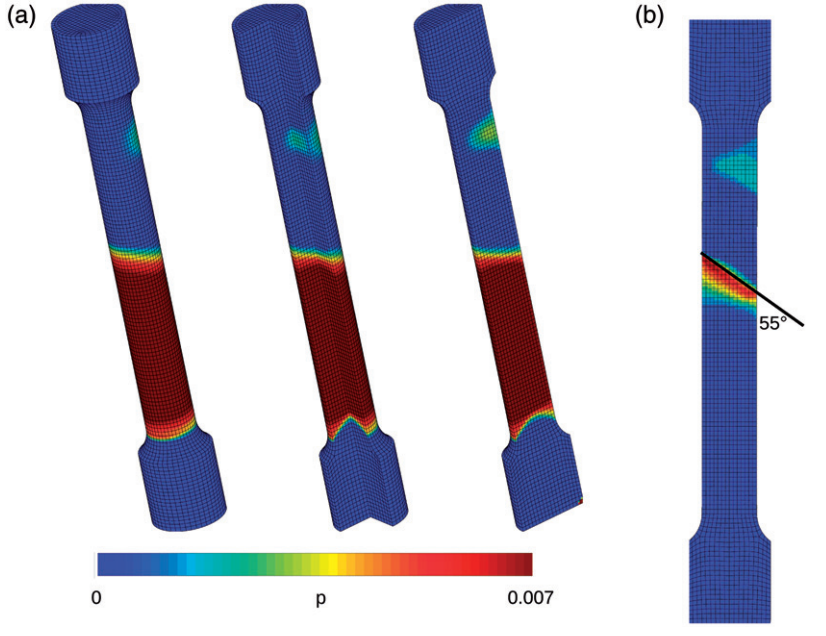

Figure 20. (a) Evolution of cumulated plastic strain at the strain rate $10^{-3}\,s^{-1}$ with the boundary conditions of Figure 18b. (b) Section of the specimen with the plastic strain rate field to measure the band orientation with respect to the tensile axis.

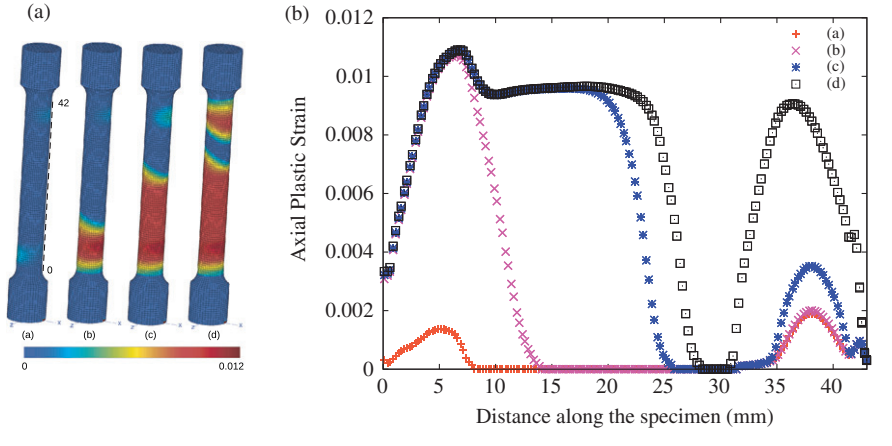

Figure 21. Plastic strain profiles along a vertical line drawn on the outer surface of the specimen (dotted black line) at four different stages of the progress of the Lüders bands in a tensile test at a strain rate $10^{-3}\,s^{-1}$: (a) corresponding plastic strain field; (b) plastic strain profiles.

It represents a significant improvement with respect to previous identification methods relying on systematic computationally expensive finite element simulations. The Lüders strain was determined from the strain field in cylindrical tensile specimens measured by DIC. The strain fields were accurately reproduced by the 3D

finite element simulations provided that loading imperfections are introduced to trigger instable inclined Lüders band formation.

Spurious mesh effects were evidenced in the conventional simulation of Lüders band formation and propagation which were unnoticed in the existing literature. A regularization procedure was proposed based on a strain gradient plasticity model to get rid of any mesh dependency. The introduction of a characteristic length into the model was also motivated by the observation that the Lüders band front is not associated with a sharp strain discontinuity. The physical mechanisms underlying the existence of a mm-size band front zone remain to be investigated especially regarding the cooperative deformation modes at work inside the grains of the polycrystal.

Complex strain localization phenomena take place at notches and crack tips in strain-aging materials. Accordingly, neglecting them in the design of engineering components is not without consequence regarding failure assessment. Fracture properties of the considered steel in the ductile regime and in the ductile-to-brittle transition will be reexamined considering the more precise constitutive equations derived in this work.

Acknowledgments

The authors would like to acknowledge the financial support from Electricité de France (EDF Les Renardières). Also the technical support from Willy Vincent and Christophe Sonnefraud (EDF-MMC) is greatly acknowledged for the help in performing mechanical tests and DIC. Special thanks are due to Prof. C. Berdin (University Paris-Sud) for her help and for her ideas about this work.

References

[1] G. Piobert, Mémoire de l'Artillerie (1842) p.505.
[2] W. Lüders, Dinglers Polytech J5 (1860) p.18.
[3] J. Zhang and Y. Jiang, Int. J. Plasticity 21 (2005) p.651.
[4] R.A. Elliot, E. Orowan, T. Udoguchi and A.S. Argon, Mech. Mater. 36 (2004) p.1143.
[5] M.R. Wenman and P.R. Chard-Tuckey, Int. J. Plasticity 26 (2010) p.1013.
[6] R. Nogueira de Codes, O.S. Hopperstad, O. Engler, O. Lademo, J. Embury and A. Benallal, Metall. Mater. Trans. A 42 (2011) p.3358.
[7] S. Kyriakides and J.E. Miller, J. Appl. Mech. 67 (2000) p.645.
[8] E. Corona, J.A. Shaw and M.A. Iadicola, Int. J. Solid Struct. 39 (2002) p.3313.
[9] V. Ballarin, M. Soler, A. Perlade, X. Lemoine and S. Forest, Metall. Mater. Trans. 40A (2009) p.1367.
[10] W.M. Lomer, J. Mech. Phys. Solids 1 (1952) p.64.
[11] F. Aguirre, S. Kyriakides and H.D. Yun, Int. J. Plasticity 20 (2004) p.1199.
[12] H. Louche and A. Chrysochoos, Mater. Sci. Eng. A 307 (2001) p.15.
[13] M. Soler, *Étude du vieillissement d'un acier à bake hardening: évolution des propriétés mécaniques de traction – corrélation avec la microstructure*, INSA Lyon, 1998.
[14] J.F. Butler, J. Mech. Phys. Solids 10 (1962) p.313.
[15] S. Avril, F. Pierron, M.A. Sutton and J. Yan, Mech. Mater. 40 (2008) p.729.
[16] B. Jaoul, *Étude de la plasticité et applications aux métaux*, Dunod, Paris, 1964.
[17] D.J. Dingley and D. McLean, Acta Metall. 15 (1967) p.885.
[18] A.H. Cottrell and B.A. Bilby, Proc. Phys. Soc. A 62 (1949) p.49.

[19] H. Tsukahara and T. Iung, Mater. Sci. Eng. A 248 (1998) p.304.
[20] L.P. Kubin and Y. Estrin, Acta Metall. 33 (1985) p.397.
[21] P.G. McCormick, Acta Metall. 36 (1988) p.3061.
[22] P. Hähner, Mater. Sci. Eng. A 164 (1993) p.23.
[23] M. Mazière, J. Besson, S. Forest, B. Tanguy, H. Chalons and F. Vogel, Comp. Meth. Appl. Mech. Eng. 199 (2010) p.734.
[24] C. Fressengeas, A.J. Beaudoin, M. Lebyodkin, L.P. Kubin and Y. Estrin, Mater. Sci. Eng. A 400–401 (2005) p.226.
[25] S. Varadhan, A.J. Beaudoin and C. Fressengeas, J. Mech. Phys. Sol. 57 (2009) p.1733.
[26] S. Forest, J. Eng. Mech. 135 (2009) p.117.
[27] H.B. Mühlhaus and J. Boland, Pure Appl. Geophys. 137 (1991) p.391.
[28] E.C. Aifantis, Int. J. Plasticity 3 (1987) p.211.
[29] P. Hähner, Appl. Phys. A: Mater. Sci. Process. 58 (1994) p.41.
[30] J. Besson, G. Cailletaud, J.L. Chaboche and S. Forest, *Nonlinear Mechanics of Materials*, Springer, Berlin, 2009.
[31] E. Voce, J. Inst. Metals 74 (1948) p.537.
[32] J. Besson and R. Foerch, Comp. Meth. Appl. Mech. Eng. 142 (1997) p.165.
[33] F. Garofalo, Metall. Trans. A 2 (1971) p.2315.
[34] N.A. Fleck and J.W. Hutchinson, J. Mech. Phys. Solids 49 (2001) p.2245.
[35] P. Hähner and L.P. Kubin, Solid State Phenom. 23–24 (1992) p.385.
[36] H.D. Wang, C. Berdin, M. Mazière, S. Forest, C. Prioul, A. Parrot and P. Le-Delliou, Scripta Mater. 64 (2011) p.430.
[37] S. Graff, S. Forest, J.L. Strudel, C. Prioul, P. Pilvin and J.L. Béchade, Mater. Sci. Eng. A 387–389 (2004) p.181.
[38] S. Zhang, P.G. McCormick and Y. Estrin, Acta Mater. 49 (2001) p.1087.
[39] J. Belotteau, C. Berdin, S. Forest, A. Parrot and C. Prioul, Mater. Sci. Eng. A 526 (2009) p.156.
[40] J. Besson, *Local Approach to Fracture*, Presse de l'Ecole des Mines, Paris, 2004.
[41] M. Mazière and H. Dierke, Comput. Mater. Sci. 52 (2012) p.68.
[42] L.P. Kubin and Y. Estrin, J. de Physique III 1 (1991) p.929.